Visualizing Ligand-Mediated Bimetallic Nanocrystal Formation Pathways with *In Situ* Liquid Phase Transmission Electron Microscopy Synthesis

Mei Wang,[1] Asher C. Leff,[2,3] Yue Li,[4] Taylor J. Woehl[1,*]

[1]Department of Chemical and Biomolecular Engineering, University of Maryland, College Park, MD 20742, USA

[2]Sensors and Electron Devices Directorate, Combat Capabilities Development Command, United States Army Research Laboratory, Adelphi, MD 20783, USA

[3]General Technical Services, LLC, Wall, New Jersey 07727

[4]Department of Chemistry & Biochemistry, University of Maryland, College Park, MD 20742, USA

[*]Corresponding author, email: tjwoehl@umd.edu

Abstract

Colloidal synthesis of alloyed multimetallic nanocrystals with precise composition control remains a challenge and a critical missing link in theory-driven rational design of functional nanomaterials. Liquid phase transmission electron microscopy (LP-TEM) enables directly visualizing nanocrystal formation mechanisms that can inform discovery of design rules for colloidal multimetallic nanocrystal synthesis, but it remains unclear whether the salient chemistry of the flask synthesis is preserved in the extreme electron beam radiation environment during LP-TEM. Here we demonstrate controlled *in situ* LP-TEM synthesis of alloyed AuCu nanoparticles while maintaining the molecular structure of electron beam sensitive metal thiolate precursor complexes. *Ex situ* flask synthesis experiments showed that nearly equimolar AuCu alloys formed from heteronuclear metal thiolate complexes, while gold-rich alloys formed in their absence. Systematic dose rate-controlled *in situ* LP-TEM synthesis experiments established a range of electron beam synthesis conditions that formed alloyed AuCu nanoparticles with similar alloy composition, random alloy structure, and particle size distribution shape as those from *ex situ* flask synthesis, indicating metal thiolate complexes were preserved under these conditions. Reaction kinetic simulations of radical-ligand reactions revealed that polymer capping ligands acted as effective hydroxyl radical scavengers during LP-TEM synthesis and prevented metal thiolate oxidation at low dose rates. *In situ* synthesis experiments and *ex situ* atomic scale imaging revealed that a key role of metal thiolate complexes was to prevent copper atom oxidation and facilitate formation of prenucleation cluster intermediates. This work demonstrates that complex ion precursor chemistry can be maintained during LP-TEM imaging, enabling probing nanocrystal formation mechanisms with LP-TEM under reaction conditions representative of *ex situ* flask synthesis.

Keywords: liquid phase transmission electron microscopy, nanoparticle synthesis, capping ligands, bimetallic nanoparticles, electron beam, transmission electron microscopy, alloys

Alloyed metal nanoparticles have received sustained attention due to their enhanced functional properties compared to monometallic nanoparticles for applications in optical devices,[1, 2] catalysis,[3-5] magnetic materials,[6, 7] and renewable energy.[8-10] Despite these broad applications, controlled colloidal synthesis of bimetallic alloys with desired structure and composition is difficult due to the varying reduction kinetics of different metal precursors, inter-metal electron transfer, and immiscibility of metals.[11] The lack of colloidal synthesis methods that enable arbitrary control over alloyed nanoparticle composition represents a bottleneck in realizing theory driven discovery of catalyst nanoparticles.[12] For instance, rational discovery of alloyed bimetallic (electro)catalyst nanoparticles involves density functional theory (DFT) prediction of alloy compositions with optimal binding energies to reaction intermediates.[13, 14] A critical missing piece to this approach is the capability to synthesize alloyed nanoparticles with arbitrary metal combinations and compositions to target DFT predicted catalytically active alloys.

The use of complex ions containing two metal sites as precursors, such as metal-capping ligand complexes,[15-19] double ionic salts,[20, 21] and molecular complexes formed by metallophilic interactions,[22] has been shown to encourage formation of bimetallic alloy nanocrystals.[23, 24] For instance, heteronuclear metal thiolate complexes have been shown to enhance copper alloying with gold in AuCu bimetallic nanoparticles.[16] Metal-ligand complexes have been shown to prevent Ostwald ripening during synthesis of alloyed FeCo bimetallic nanoparticles.[23] Selective binding of metal ions to ligands can also be used to rationally manipulate and harmonize the reduction kinetics of metal precursors.[25] Use of complex ions as precursors points to a facile approach to

nanoparticle synthesis, where capping ligands actively control nanocrystal properties and final nanoparticle characteristics (*e.g.* composition and alloy structure) are directly encoded into the molecular scale precursor chemistry *via* rationally designed coordinate bonds, reduction potentials, and metal-metal bonds.

While systematic synthesis and x-ray scattering experiments have revealed crucial chemical processes underlying formation of bimetallic nanoparticles,[26-30] the specific chemical processes involved in conversion of complex ion precursors to bimetallic alloys remain unclear. A prevailing hypothesis is that multimetallic precursor complexes confine metal species together and facilitate alloying starting from the molecular level.[16] However, beyond this qualitative description it is unclear how capping ligands impact chemical processes underlying nanoparticle formation, including precursor reduction, nucleation, and growth. Liquid phase transmission electron microscopy (LP-TEM) directly visualizes nanoparticle formation in real time at atomic to nanometer scale spatial resolution.[31-34] Further, LP-TEM experiments harnessing controllable electron beam chemistry enable systematically varying synthesis conditions, *e.g.* redox chemistry and reaction kinetics, to directly observe the impacts on nanoparticle formation mechanisms.[34-40] However, there remains the challenge of demonstrating the chemistry involved in LP-TEM electron beam synthesis is representative of bench scale wet chemistry.[41] Ideally, the electron beam should only reduce metal precursors and not drive undesirable side reactions like oxidation of organic capping ligands or nanoparticles.[42, 43] In this article, we reveal *in situ* LP-TEM electron beam synthesis conditions for alloyed bimetallic nanoparticles that preserve the salient chemistry of the *ex situ* flask synthesis (**Figure 1a**). We chose AuCu alloyed nanocrystals as a model system because of their important application as a highly active CO_2 electroreduction catalysts.[44-46] Prior work has shown that although AuCu alloys are thermodynamically favorable through intermetallic

phase formation,[47-50] it is challenging to synthesize alloyed AuCu nanocrystals with tunable composition by wet chemical co-reduction due to the different reduction kinetics of gold and copper precursors. In this article, we use alloying extent and nanoparticle characteristics as sensitive electron beam damage indicators, where formation of equimolar, unaggregated AuCu alloy nanocrystals indicated metal thiolate complex integrity was preserved during *in situ* LP-TEM synthesis. Radical-ligand reaction kinetic simulations go beyond empirical observations of electron beam damage to demonstrate how polymeric capping ligands act as effective radical scavengers that protect metal thiolate complexes from oxidation. Broadly, this study demonstrates that systematic LP-TEM experiments can probe chemical processes involved in multicomponent nanoparticle formation while preserving the relevant inorganic chemistry of the *ex situ* flask synthesis.

Results and Discussions

Ex situ and in situ synthesis of AuCu nanocrystals

Bimetallic AuCu nanoparticles were synthesized by *ex situ* flask synthesis using a previous synthesis method.[16] Briefly, an aqueous metal thiolate complex precursor was prepared by mixing polyethylene glycol thiol (PEG-SH, average molecular weight of 775 g/mol), gold chloride ($HAuCl_4$), and copper nitrate ($Cu(NO_3)_2$) (see details in **Experimental Methods**). Matrix assisted laser desorption/ionization time of flight mass spectroscopy (MALDI-TOF MS) showed that pentanuclear metal thiolate complexes containing both gold and copper formed upon mixing, together with some residual PEG-SH (**Figure 1b**).[16, 19] Prior reports have shown formation of tetranuclear complexes using the same method, albeit with a larger polymer molecular weight of 1000 g/mol.[16] It is possible that a larger complex formed in this study due to the lower polymer

molecular weight, which exhibit reduced steric effects and a lower configurational entropic penalty for polymer complexation, enabling formation of a larger complex.[51] In *ex situ* flask synthesis, an aqueous solution of metal thiolate complexes was reduced by a slight excess of sodium borohydride at room temperature. *In situ* LP-TEM synthesis was carried out utilizing the electron beam to create reducing radical species (**Figure 1a**), where continuous irradiation by the scanning TEM (STEM) electron beam generated reducing aqueous electrons (e_{aq}^-) and hydrogen radicals ($H\cdot$) through radiolysis.[33, 52] Dose rate ($\dot{d}$), the amount of energy absorbed by the liquid sample per unit mass per unit time in units of Gray/s (Gy/s), determined the concentration of radicals and was modified during *in situ* LP-TEM synthesis by changing the image magnification ($\dot{d} \propto M^2$) and electron beam current ($\dot{d} \propto i_e$).[34, 35, 53] Reducing radicals have higher standard reduction potentials ($E_{H\cdot}^0 = -1.9\ V$; $E_{e_{aq}^-}^0 = -2.3\ V$) compared to sodium borohydride ($E_{BH_4^-}{}^0 = -0.48\ V$), indicating they are stronger reducing agents.[41, 54] To account for this, we modified the precursor composition for *in situ* LP-TEM synthesis by carrying out systematic LP-TEM experiments at various precursor dilutions. We found *in situ* LP-TEM synthesis with a precursor solution diluted by 7 times formed densely packed overlapping nanoparticles, while a precursor diluted 70 times formed no nanocrystals (**Figure S1**). *In situ* LP-TEM synthesis using a precursor diluted by 35 times formed isolated nanocrystals under most conditions and was used for the study.

We carried out *in situ* LP-TEM synthesis experiments at various dose rates to probe the effect on nanocrystal formation dynamics and final size, morphology, and composition. Time lapsed LP-TEM images of nanocrystal formation at a relatively low dose rate of 17 MGy/s ($[e_{aq}^-] = 2.9\ \mu M$ and $[H\cdot] = 4.6\ \mu M$) formed sub-10 nm nanocrystals through continuous nucleation and growth over ~30 s (**Figure 2a**). The nanocrystals were spherical and ellipsoidal with final diameters ranging from a few to ten nanometers, showed uniform image contrast, and

were not mobile during formation due to heterogeneous nucleation on the silicon nitride membrane.[55] At a higher dose rate of 65 MGy/s ($[e_{aq}^-] = 4.3$ μM and $[H\cdot] = 8.9$ μM), irregularly shaped, aggregated nanoparticles formed from the beginning of synthesis (**Figure 2b**). The image contrast of the nanoparticles was non-uniform with each particle displaying high and low image contrast regions within. *In situ* synthesis in the absence of PEG-SH ligand formed large, abnormally shaped nanoparticles that had non-uniform internal image contrast similar to nanoparticles formed at high dose rates with ligand (**Figure 2c**).

Nanocrystal morphology and composition

The resolution limit of LP-TEM was 1-2 nm in the *in situ* experiments so the atomic structure and composition of individual nanocrystals were characterized with high resolution TEM (HRTEM), high-angle annular dark-field scanning transmission electron microscopy (HAADF-STEM), and energy dispersive x-ray spectroscopy (EDS) on nanocrystals after removing them from the LP-TEM holder and drying the liquid. AuCu nanocrystals synthesized in a flask were nearly spherical and 2 – 4 nm in diameter (**Figures 3a, 3e, and Figure S2a**). In comparison, nanocrystals synthesized at a low dose rate of 7.3 MGy/s were nearly spherical, single crystal, and had diameters ranging from 2 – 10 nm (**Figures 3b, 3f, and Figure S2b**). Nanocrystals synthesized at a high dose rate of 210 MGy/s were a mixture of polycrystalline aggregates and single crystal particles with sizes < 2 nm (**Figures 3c, 3g, and Figure S2c**). For all dose rates tested, nanocrystals synthesized with no PEG-SH ligand were abnormally shaped polycrystalline aggregates larger than 20 nm (**Figures 3d, 3h and Figure S2d**). STEM-EDS showed that nanocrystals formed by *ex situ* flask synthesis and low dose rate *in situ* LP-TEM synthesis (< 25 MGy/s) were alloyed with gold contents ranging from 59 – 66 atomic% and 49 – 53 atomic%, respectively (**Figures 3i-k and**

Figures S3a-e). Due to the quantification error in the EDS data (See methods for EDS quantification details), we cannot establish that these alloy compositions were statistically different. Nanocrystals formed at high dose rates and without PEG-SH capping ligands were predominantly gold with only traces of copper (< 5 atomic%) **(Figure S3f,g)**. As a negative control for *ex situ* flask synthesis with no metal thiolates, nanocrystals were synthesized from metal thiolate complexes that were first oxidized with hydrogen peroxide (H_2O_2) to form a physical mixture of metal ions, PEG-SH, and disulfide bonded PEG (see **Section 4** in **Supplementary Information** and **Figure S4a**). The nanocrystals formed from the oxidized precursor showed a significant decrease in copper content with compositions ranging from 80 – 90 atomic% gold (**Figure 3k, Figure S3h,i and Figure S4c**). Atomic resolution HAADF-STEM imaging showed that nanocrystals formed with low dose *in situ* LP-TEM synthesis were single crystalline and co-existed with small (< 1 nm) non-crystalline metal clusters (**Figure 3l**). Lattice constants for AuCu nanocrystals formed by low dose rate *in situ* and *ex situ* synthesis were both near 3.9 Å (**Figure S5)**, between that of Au and Cu, indicating the nanocrystals were random AuCu alloys.

Quantification of particle size distribution and aggregation state

Flask-synthesized nanocrystals ranged in diameter from 1 – 4 nm and the particle size distribution (PSD) had a shoulder centered around the mean particle diameter of ~2 nm (**Figure 4a**). The *in situ* synthesized nanocrystals had diameters ranging from 2 – 10 nm and similarly showed a shoulder in the PSD near the average particle size of ~4 nm for dose rates of < 17 MGy/s (**Figure 4a**, blue curve). The PSD shoulder disappeared at larger dose rates and was accompanied by formation of aggregated particles with sizes > 5 nm and single crystal particles with sizes < 2 nm. Direct comparison of the PSDs of the *in situ* and *ex situ* synthesized nanocrystals was not

possible due to the continuous nature of *in situ* synthesis where the reaction time determines the particle size.[56, 57] However, the reduced PSDs (particle size normalized to the average particle size) for low dose rate (< 17 MGy/s) *in situ* and *ex situ* synthesis had nearly identical shape and shoulder position (**Figure S6c**). Similar reduced PSD shape and reduced size range for *in situ* and *ex situ* synthesis indicates a common growth mechanism.[56, 58, 59] These results indicate a different reaction rate or time for *in situ* and *ex situ* synthesis but a common growth mechanism.

The degree of nanocrystal aggregation for each synthesis condition was quantified by particle eccentricity (e), a measure of how spherical a shape is with $e = 0$ being a perfect circle, $e = 1$ a line, and values in between corresponding to ellipses of increasing aspect ratio. **Figure 4b** shows the particle eccentricity distributions for *in situ* LP-TEM synthesis at different dose rates compared to *ex situ* flask synthesis. Most particles formed by *ex situ* flask synthesis had eccentricities ranging from $e = 0.3 - 1$, indicating nearly spherical particles formed together with some aggregates and non-spherical particles. The eccentricity of the nanoparticles formed by *in situ* LP-TEM synthesis was smaller overall compared to *ex situ* flask synthesis for dose rates < 17 MGy/s and increased with increasing dose rate above the flask synthesized particles for dose rates > 34 MGy/s. **Figure 4c** shows a heat map of the median particle eccentricity for 11 unique *in situ* LP-TEM synthesis dose rates (see **Section 6** in **Supplementary Information** for details on heat map generation). To quantify the fraction of aggregated nanocrystals under each *in situ* LP-TEM synthesis, particles with e > 0.75 were classified as aggregates to generate a heat map of aggregated fraction (**Figure 4d**; see **Section 6** in **Supplementary Information** and **Figure S6** for additional details on aggregate classification). At high beam currents and magnifications (red/orange areas), more than half the particles were classified as aggregates. Less than a third of the particles were aggregates at low beam current and magnification (blue and teal areas), similar

to *ex situ* flask synthesized nanocrystals. In terms of alloy composition, PSD and reduced PSD shape, alloy structure, and aggregation, particles formed by *in situ* LP-TEM synthesis at dose rates < ~20 MGy/s were most representative of particles synthesized by *ex situ* flask synthesis.

Radical-ligand reactions

Given the impact of PEG-SH ligands and dose rate used for *in situ* LP-TEM synthesis on the characteristics of the AuCu nanocrystals, we explored radical-ligand chemical reactions using reaction kinetic simulations. In addition to aqueous electrons and hydrogen radicals, strongly oxidizing hydroxyl radicals ($OH\cdot$, E^0 = +2.8 V) form during water radiolysis.[35, 53] Hydroxyl radicals, aqueous electrons, and hydrogen radicals react rapidly with PEG and thiol functional groups (**Figure 5a**). Hydroxyl and hydrogen radicals abstract hydrogen from the thiol functional groups to form thiyl radicals, $PEG-S\cdot$. Aqueous electrons sever the C-S bond between the PEG and thiol, creating a reactive alkyl radical at the end of the PEG chain, $PEG\cdot$.[60, 61] $PEG-S\cdot$ species are rapidly oxidized by dissolved oxygen[62] into $PEG-SOO\cdot$ or recombine to form disulfide bridges (PEGS-SPEG).[63] Besides the thiol functional group, hydroxyl radicals readily oxidize the PEG chain *via* hydrogen abstraction to form alkyl radicals on the PEG chain, $PEG\cdot-SH$.[64]

Based on the above reactions, we developed a diffusion-reaction kinetic model for the radical-ligand reactions that calculates the concentration of each radical and ligand species as a function of spatial position within the LP-TEM image area, time, and dose rate (see **Methods**, **Section 7** in **Supplementary Information**, **Figure S7**, **Table S1** for additional details on the radical-ligand reaction model). **Figure 5b** shows the steady state concentration of hydroxyl radicals and significant ligand damage products for a dose rate of 7.3 MGy/s. The kinetics reached steady state in less than a second (**Figure S8**) and the concentration of each species was nearly

uniform across the radiation area, consistent with our LP-TEM observations of uniform nanocrystal size (*cf.* **Figure 2a**). The simulation showed that 25.8% of the initial PEG-SH ligands were converted to $PEG-S\cdot$, 54.6% to $PEG\cdot$, and 10% to PEGS-SPEG. The concentration of each species at the center of image area was computed as a function of dose rate and showed that the PEG-SH and PEGS-SPEG concentrations decreased as a function of increasing dose rate, PEG-S· concentration increased slightly, and $PEG\cdot$ concentration remained nearly constant (**Figure 5c**). The OH· concentration increased by nearly an order of magnitude when increasing dose rate from 7.3 MGy/s to 210 MGy/s.

Preserving nanocrystal precursor chemistry during LP-TEM

Our experiments showed AuCu nanocrystals formed by *ex situ* flask synthesis and *in situ* LP-TEM synthesis at dose rates < 20 MGy/s both showed nearly equimolar alloy composition, random alloy structure, and similar PSD shape and aggregation states (**Figures 3 and 4**). Conversely, nanocrystals formed by high dose rate *in situ* LP-TEM synthesis and *ex situ* flask synthesis from H_2O_2 oxidized metal thiolate complexes were gold rich with less copper integration in the nanocrystals compared to those made from intact complexes (**Figure 3j,k** and **Figure S3, S4**). These results have several implications for LP-TEM visualization of nanocrystal formation and the role of complex ion precursors in forming alloyed nanocrystals. *Ex situ* flask synthesis showed that metal thiolate complexes were essential to integrating significant amounts of copper into alloyed AuCu nanocrystals, with results showing a significant decrease in copper content after metal thiolate complexes were first oxidized with H_2O_2 (**Figure 3k**). This indicates that intact metal thiolate complexes were a necessary prerequisite to synthesize alloyed AuCu nanoparticles with significant integration of copper into the alloy.[16] Despite over 90% of the PEG-SH capping

ligands being modified by radical reactions, alloyed AuCu nanocrystals with nearly equimolar composition were formed by low dose rate *in situ* LP-TEM synthesis, indicating metal thiolates were preserved. These experiments established limits on the spatial resolution this specific nanocrystal synthesis can be visualized with LP-TEM while retaining the essential chemistry of the *ex situ* flask synthesis. Above the threshold dose rate of 20 MGy/s, electron beam generated radicals significantly altered the solution chemistry compared to *ex situ* flask synthesis, leading to a significantly different nanocrystal formation pathway and final nanocrystal product during LP-TEM. This indicates it was not possible to image this nanocrystal formation process at atomic resolution under conditions representative of *ex situ* flask synthesis, as the required dose rate for atomic resolution imaging is > 2500 MGy/s. The threshold dose rate for preserving native precursor chemistry during LP-TEM imaging is expected to vary as a function of nanoparticle material, ligand, solvent, presence of radical scavenger, and type of liquid cell membrane used (*e.g.* silicon nitride or graphene). For instance, a recent LP-TEM study on silver metal-organic nanotube formation mechanism, which involved reaction of di-triazole ligands and silver ions (both are sensitive to oxidation), empirically found that damage free *in situ* synthesis was achieved for a dose rate of ≤ 1.6 MGy/s.[65] Rigorously establishing *in situ* LP-TEM synthesis conditions where nanocrystals form with similar structure and chemistry compared to *ex situ* flask synthesis is critical to confidently translate mechanisms learned from LP-TEM experiments to understand chemical processes occurring during *ex situ* flask synthesis.

Given the extreme radiation environment of *in situ* LP-TEM synthesis and the simulation results showing >90% of PEG-SH capping ligands were modified by radiolysis, the question remains, how were metal thiolate complexes preserved at low dose rates? The formation of gold rich particle aggregates at high dose rate leads us to hypothesize that the electron beam chemically

modified metal thiolate complexes and free PEG-SH ligands, rendering them less effective at stabilizing nanoparticles and encouraging alloying. Radical-ligand reaction simulations showed that PEG-SH was an effective hydroxyl radical scavenger at low dose rates that prevented oxidative damage of metal thiolate complexes. Kinetic simulations showed that at dose rates < 20 MGy/s, the concentration of hydroxyl radicals was an order of magnitude lower than at high dose rates of > 200 MGys (*cf.* **Figure 5c**). The most significant scavenging reactions were hydrogen abstraction from thiol groups and the PEG carbon chain due to their large rate constants (**Table S1**). Interestingly, several of the scavenging reaction products retained their ability to act as capping ligands; PEG-S· is an intermediate in the formation of metal-sulfur anchoring bonds between thiol groups and metal nanocrystal surfaces,[66, 67] while disulfide groups (PEGS-SPEG) are weakly binding capping ligands.[68] Hydroxyl radical concentration increased with increasing dose rate and as PEG-SH was depleted, oxidized coordinate bonds in the metal thiolate complexes, copper atoms, and metal-sulfur bonds that anchor capping ligands to nanocrystal surfaces. The nanocrystals synthesized *ex situ* from the oxidized metal thiolate complex precursor, where H_2O_2 acted as a surrogate for hydroxyl radicals, had increased polydispersity and size and decreased copper content (**Figure S4**), reminiscent of the nanocrystals formed by high dose rate *in situ* LP-TEM synthesis. Oxidation of metal-sulfur bonds at the capping ligand-nanoparticle interface reduced surface ligand coverage and the colloidal stability of nanocrystals, causing them to aggregate during *in situ* LP-TEM synthesis at high dose rate (*cf.* **Figure 2b**).

While we do not know the exact reaction pathways for oxidation of the metal thiolate complexes by hydroxyl radicals, *ex situ* oxidation of metal thiolate complexes with H_2O_2 produced a physical mixture of PEG-SH and PEGS-SPEG (**Figure S4a**) and metal ions not complexed to thiol ligands. This result suggests metal thiolate complex oxidation during high dose rate *in situ*

LP-TEM synthesis released free (not ligand complexed) gold and copper ions into solution. Co-reduction of a physical mixture of copper and gold ions by *in situ* LP-TEM synthesis formed nearly pure gold nanoparticles (**Figure S3g**), while similar gold rich nanocrystals formed by *ex situ* flask synthesis from the H_2O_2 oxidized precursor. A high reduction rate of gold ions compared to copper, inter-metal electron transfer from copper to gold,[69, 70] and oxidation of copper by hydroxyl radicals led to preferential reduction of gold into nearly monometallic nanoparticles at high dose rate.

Formation mechanism of alloyed AuCu nanocrystals

Controlled *in situ* LP-TEM synthesis while maintaining the metal thiolate complex chemistry enabled probing the role of metal thiolate complexes in the nanocrystal formation mechanism. Alloyed nanoparticles formed by *in situ* synthesis had nearly equimolar gold and copper contents and size invariant composition within the error of EDS quantification ($\pm$5 – 10 atomic%) (**Figure 3j,k**, **Figure S3a,b** and **Figure S9**).[71, 72] A size invariant alloy composition indicates that the gold and copper attachment rates to the nanoparticle surface were constant as a function of synthesis time (**Figure S3c**). Past studies have identified small (< 1 nm) mixed metal clusters and thiolated metal prenucleation clusters as critical intermediate species during synthesis of monometallic, bimetallic, and semiconductor nanocrystals.[73-77] Atomic resolution HAADF-STEM imaging provided direct evidence for the formation of sub-nanometer metal clusters during *in situ* LP-TEM synthesis (*cf.* **Figure 3l**). Prior DFT calculations have shown that bimetallic metal clusters are energetically favorable compared to monometallic clusters due to the favorable negative Gibb's free energy of mixing.[73] Thermodynamically stable bimetallic clusters have been predicted or experimentally measured for several metal combinations, including AgAu, AuPd, PdCo, AgCu, and AgNi.[78-81] EDS measurements of constant alloy composition, HAADF-STEM imaging of sub-nanometer metal clusters, and prior DFT calculations provide compelling evidence

supporting mixed metal prenucleation clusters as intermediates that fix attachment rates of each metal to the nanocrystal surface (*cf.* **Figure 3k,l**). These results further suggest that metal thiolates prevent preferential reduction of gold by limiting inter-metal electron transfer *via* simultaneous reduction of copper and gold and aggregation into mixed metal prenucleation clusters.

Based on our systematic *in situ* and *ex situ* synthesis experiments, HRTEM characterization, and kinetic modeling of radical-ligand reactions, we propose an overall mechanism for ligand- and dose rate-mediated AuCu nanocrystal formation (**Figure 6**). At low dose rates (< 20 MGy/s), PEG-SH acted as a capping ligand and a OH· radical scavenger that protected metal thiolate complexes, copper atoms, and metal-sulfur ligand anchoring bonds from oxidative attack. Metal thiolate complexes were reduced to bimetallic prenucleation metal clusters that served as intermediates to AuCu nanocrystals. The surface of bimetallic AuCu nanocrystals were stabilized by PEG-SH and other ligand damage products, which prevented them from aggregating. At high dose rate, large concentrations of OH· radicals overwhelmed the scavenging capacity of the PEG-SH and oxidized metal thiolate complexes, releasing free copper and gold ions into solution.[82] Copper atoms were oxidized by either OH· radicals or gold ions, leading to preferential reduction of gold and formation of nearly pure gold nanocrystals. Depletion of ligands and oxidation of metal-sulfur bonds destabilized nanocrystals and caused aggregation.

Conclusions

Systematic *in situ* and *ex situ* synthesis, reaction kinetic simulations, and extensive characterization demonstrated low dose rate *in situ* LP-TEM synthesis of alloyed AuCu nanocrystals while preserving the chemistry of heteronuclear metal thiolate complexes. This result was unexpected based on the extreme levels of ionizing radiation present during *in situ* LP-TEM

synthesis (dose rates in LP-TEM are 10^4-10^5 times larger than in a nuclear reactor). Characterization of nanocrystals formed by *in situ* synthesis rigorously identified low dose rate conditions (< 20 MGy/s) that formed alloyed nanocrystals of similar shape of PSD, random alloy structure, and similar equimolar of Au and Cu content compared to *ex situ* flask synthesis. Alloyed AuCu nanoparticles had size invariant composition and nearly equimolar alloy composition, indicating the molecular structure of the metal thiolate complex was not significantly damaged by radicals at low dose rate. A radiolysis kinetic model was developed to understand electron beam damage of organic capping ligands and revealed that PEG-SH ligands were effective hydroxyl radical scavengers at low dose rates, preventing oxidation of metal thiolate complexes. Preferential gold reduction and formation of gold rich nanoparticles at high dose rates and in the absence of metal thiolate complexes demonstrated the importance of metal thiolate complexes in preventing copper oxidation by inter-metal electron transfer and forming sub-nanometer metal cluster intermediate species. These results suggest a method for tuning the alloy composition of nanocrystals during flask synthesis by either changing the composition of the precursor complex or adding oxidizing species together with the reducing agent to control solution concentrations of free metal ions and metal thiolates and thus the relative rates of metal reduction, prenucleation cluster formation, and inter-metal electron transfer.

Methods/Experimental

Precursor solution preparation

Precursors solutions were prepared following a prior method with minor modifications.[16] Stock solutions of 20 mM chloroauric acid ($HAuCl_4$, Sigma-Aldrich, 99.99%), 20 mM copper nitrate ($Cu(NO_3)_2$, Sigma-Aldrich, ACS, 98%), and 10 mM PEG-SH (Sigma-Aldrich, average M_n

= 800 g/mol) were prepared with deionized water (18.2 MΩ). The precursor solution used for *ex situ* flask synthesis was prepared by adding 94 μL of 20 mM $HAuCl_4$ and 94 μL of 20 mM $Cu(NO_3)_2$ solution to 4.29 mL DI water with stirring, followed by adding 376 μL of 10 mM PEG-SH solution. The precursor solution used for *in situ* LP-TEM synthesis was prepared by adding 2.5 μL of 20 mM $HAuCl_4$ solution and 2.5 μL of 20 mM $Cu(NO_3)_2$ to 4.99 mL DI water degassed for one hour by sonication (Bransonic, CPX2800H), followed by adding 10 μL of 10 mM PEG-SH solution. Both precursor solutions had a molar ratio of Au:Cu:PEG-SH of 1:1:2. The precursors were characterized by matrix-assisted laser desorption/ionization time of flight mass spectrometer (MALDI-TOF MS).

MALDI-TOF MS

The MALDI-TOF MS experiments were performed with a Bruker Autoflex Speed MALDI-TOF. Samples were prepared by adding 23.5 µL of 20 mM HAuCl4, 23.5 µL of 20 mM $Cu(NO_3)_2$ and 94 μL of 10 mM PEG-SH solution to 1072 µL DI water to form metal thiolate complex solution. 10 μL of the metal thiolate complex solution was mixed with 10 μL of 20 mg/mL 2,5-Dihydroxybenzoic acid (DHB) solution and 1 μL of 10 mg/mL NaCl in 1:1 methanol/DI water solution to form the targeted solution. 1 μL of targeted solution was drop-cast onto the MALDI plate and air dried for 10 minutes. The system was operated in linear positive mode.

Ex situ flask synthesis of bimetallic nanocrystals from metal thiolate complex precursors

Bimetallic nanocrystals were synthesized by reducing the precursor solution at room temperature with sodium borohydride. Immediately after the addition of PEG-SH to the metal

precursors, 450 μL of 20 mM $NaBH_4$ solution was quickly added to the flask with vigorous stirring at room temperature. The reaction was run for one hour under strong magnetic stirring. The synthesized nanocrystals were then washed with DI water 5 times using a 10 kDa protein concentrator. To synthesize nanocrystals from an oxidized metal thiolate precursor, 0.5 μL H_2O_2 (30 % (w/w) in H_2O) solution was added immediately after the formation of metal thiolate complex and stirred for 4 hours at room temperature. The oxidized precursor solution was then reduced with $NaBH_4$ under identical conditions as described above.

In situ LP-TEM synthesis of bimetallic nanocrystals

All LP-TEM experiments were performed with a Protochips liquid cell holder (Poseidon Select), which utilizes two silicon chips with 50 nm freestanding silicon nitride membranes to contain a thin electron transparent film of liquid. The nominal thickness of the liquid film was 500-750 nm due to the flow spacers (150 nm) and membrane bulging. The window areas of both chips were 550 µm × 50 µm. Before the experiments, both chips were sequentially rinsed with acetone, methanol and DI water, and then plasma cleaned (Harrick Plasma, PDC-32G) for 3 minutes with an 18 W air plasma to remove organic contamination and render the chip surface hydrophilic. 2 µL of prepared precursor solution was drop-cast between the silicon chips before assembling the sample. After assembling the cell, precursor solution was continuously flowed through the cell for ~15 minutes at a flow rate of 300 µL/h to remove any bubbles from the cell. All imaging was performed on a JEOL JEM-2100F TEM in STEM mode with an accelerating voltage of 200 kV. Each *in situ* LP-TEM synthesis experiment was performed along the edge of the silicon nitride membrane to maintain constant liquid thickness, with 5 µm separating each experiment. Precursor

solution was flowed for 5 minutes at a flowrate of 300 µL/h between each new experiment in the same sample cell, in order to replenish precursor to avoid depletion effects.[83, 84]

Sample preparation for TEM characterization

The *ex situ* flask synthesized particles dispersed in DI water were drop-casted onto a nickel TEM grid. Most of the droplet was wicked off prior to drying on the TEM grid to avoid artificial aggregation by capillary forces. The TEM grids were plasma cleaned in an air plasma for 3s before TEM characterization. Nanocrystals formed by *in situ* LP-TEM synthesis were characterized dry with HRTEM, HAADF-STEM, and STEM-EDS. Following the LP-TEM experiment, the silicon nitride chips were removed from the liquid cell holder and rinsed with DI water to remove residual precursor and allowed to dry in air. The chip was plasma cleaned in an air plasma for one minute to remove contamination prior to TEM characterization.

TEM characterization

STEM-EDS quantification of alloy composition was performed on a JEOL JEM-2100F TEM operating in STEM mode at 200 kV, using a SiLi X-ray detector (Oxford Instruments). After locating a nanocrystal in HAADF-STEM imaging mode, an image was taken and then EDS spectra were acquired at every 0.5 nm along a ~20 nm line through the nanocrystal center. EDS spectra were acquired and integrated over about 3 minutes to minimize sample drift, contamination, and electron beam damage. To accrue enough counts for quantification, EDS spectra along each line scan were summed into a single spectrum. The weight fraction of each metallic element was quantified from each EDS spectrum using the Cliff-Lorimer equation, $\frac{C_{Au}}{C_{Cu}} = k_{Aucu}\frac{I_{Au}}{I_{Cu}}$,[85] where I_{Au} and I_{Cu} represent the integrated characteristic X-ray intensities of gold and copper. The

integrated characteristic X-ray intensities were determined by background subtracting the EDS spectra and then integrating the characteristic X-ray peak. EDS quantification of gold used the AuL_α emission line at 9.712 keV, while Cu quantification used the CuK_α emission line at 8.040 keV. k_{Aucu} is the sensitivity factor and can be calculated from the first principles, $k_{Aucu} = A_{Au}w_{Cu}Q_{Cu}a_{Cu}e_{Cu}/A_{Cu}w_{Au}Q_{Au}a_{Au}e_{Au}$, where A_{Au} and A_{Cu} represent the atomic weight of Au and Cu elements, w_{Au} and w_{Cu} represent the L-shell fluorescence yield of gold and K-shell fluorescence yield of copper respectively. Q_{Au} and Q_{Cu} represent the electron ionization cross sections for L-shell of gold element and K-shell of copper elements. a_{Au} and a_{Cu} represent the ratio of AuL_α radiation to total Au x-ray shell intensity and a_{Cu} represents the ratio of CuK_α radiation to total Cu x-ray intensity. e_{Au} and e_{Cu} represent the EDS detector efficiency of gold and copper elements respectively.[86] The above quantification analysis was performed with the INCA software package from Oxford Instruments. The error bars in the quantification results are due to background noise in individual EDS measurements from each particle. Atomic resolution HAADF-STEM imaging was performed on a spherical aberration corrected JEOL ARM200F at 200 kV accelerating voltage.

Radiolysis simulations

The radiolysis model for radical-ligand reactions is a modified version of the original radiolysis model developed by Schneider *et al.*[53] The original model accounts for the 79 recombination reactions between electron beam induced radicals. The current model adds 17 radical-ligand reactions and accounts for diffusion of species into and out of the irradiation area. While more than 17 reactions occur between the capping ligands and electron beam generated radicals, these reactions were included because they had significant reaction rate constants (>10^8 $M^{-1}s^{-1}$). Reactions were compiled from literature values for small molecule alkyl thiols and

aqueous PEG solutions.[60-64, 87] In short, radical species are continuously and homogenously generated in the LP-TEM image area due to energy deposited by the electron beam with a defined dose rate. Radicals either recombine, react with capping ligands, or diffuse out of the image area. The balance of these processes leads to a steady state concentration of radical species, ligands, and ligand damage products after less than a second of irradiation. Due to the absence of rate constants for radical reactions with metal ions, we ignore these reactions in the model. The model was implemented in COMSOL using the transport of dilute species module. See **Section 7** in **Supplementary Information** for additional details. The COMSOL model file is available upon reasonable request.

ASSOCIATED CONTENT

Supporting information

The *Supporting Information* is available free of charge on the ACS Publications website at DOI:XXX. Supporting information includes: optimal metal thiolate complex concentration for *in situ* LP-TEM synthesis; HRTEM images of nanocrystals formed by *in situ* LP-TEM and *ex situ* flask synthesis; *ex situ* flask synthesis and MALDI-TOF of oxidized metal thiolate complexes; HAADF-STEM and EDS of nanocrystals formed by *in situ* LP-TEM and *ex situ* flask synthesis; FFT analysis of lattice constants of AuCu bimetallic nanocrystals; image analysis methods for particle size distribution and eccentricity; reactions for radiolysis simulations of radical-ligand reactions; quantitative HAADF STEM analysis of nanoparticle alloy composition.

ORCID

Taylor Woehl: 0000-0002-4000-8280

Acknowledgements

T.J.W and M.W. acknowledge funding from ACS PRF (#61111-DNI10).The authors acknowledge the Advance Imaging & Microscopy Laboratory (AIMLAB) at the University of Maryland.

Author Contributions

T.J.W. conceived and supervised the study. M.W. performed nanoparticle synthesis, LP-TEM experiments, HRTEM imaging, MALDI-TOF MS, and data analysis. A.C.L. performed atomic resolution HAADF-STEM imaging. Y.L. performed MALDI-TOF MS experiments. T.J.W. and M.W. wrote and edited the manuscript.

References

1. Ross, M. B.; Ku, J. C.; Lee, B.; Mirkin, C. A.; Schatz, G. C., Plasmonic Metallurgy Enabled by DNA. *Advanced Materials* **2016,** *28* (14), 2790-2794.
2. Cortie, M. B.; McDonagh, A. M., Synthesis and Optical Properties of Hybrid and Alloy Plasmonic Nanoparticles. *Chemical Reviews* **2011,** *111* (6), 3713-3735.
3. Luo, L.; Duan, Z.; Li, H.; Kim, J.; Henkelman, G.; Crooks, R. M., Tunability of the Adsorbate Binding on Bimetallic Alloy Nanoparticles for the Optimization of Catalytic Hydrogenation. *Journal of the American Chemical Society* **2017,** *139* (15), 5538-5546.
4. Goulas, K. A.; Sreekumar, S.; Song, Y.; Kharidehal, P.; Gunbas, G.; Dietrich, P. J.; Johnson, G. R.; Wang, Y. C.; Grippo, A. M.; Grabow, L. C.; Gokhale, A. A.; Toste, F. D., Synergistic Effects in Bimetallic Palladium–Copper Catalysts Improve Selectivity in Oxygenate Coupling Reactions. *Journal of the American Chemical Society* **2016,** *138* (21), 6805-6812.
5. Baber, A. E.; Tierney, H. L.; Sykes, E. C. H., Atomic-Scale Geometry and Electronic Structure of Catalytically Important Pd/Au Alloys. *ACS Nano* **2010,** *4* (3), 1637-1645.
6. Sun, S., Recent Advances in Chemical Synthesis, Self-Assembly, and Applications of FePt Nanoparticles. *Advanced Materials* **2006,** *18* (4), 393-403.
7. Abadía, M.; Ilyn, M.; Piquero-Zulaica, I.; Gargiani, P.; Rogero, C.; Ortega, J. E.; Brede, J., Polymerization of Well-Aligned Organic Nanowires on a Ferromagnetic Rare-Earth Surface Alloy. *ACS Nano* **2017,** *11* (12), 12392-12401.
8. Stamenkovic, V. R.; Mun, B. S.; Arenz, M.; Mayrhofer, K. J. J.; Lucas, C. A.; Wang, G.; Ross, P. N.; Markovic, N. M., Trends in electrocatalysis on extended and nanoscale Pt-bimetallic alloy surfaces. *Nature Materials* **2007,** *6*, 241.
9. Kim, D.; Resasco, J.; Yu, Y.; Asiri, A. M.; Yang, P., Synergistic geometric and electronic effects for electrochemical reduction of carbon dioxide using gold–copper bimetallic nanoparticles. *Nature Communications* **2014,** *5*, 4948.

10. Choi, S.-I.; Shao, M.; Lu, N.; Ruditskiy, A.; Peng, H.-C.; Park, J.; Guerrero, S.; Wang, J.; Kim, M. J.; Xia, Y., Synthesis and Characterization of Pd@Pt–Ni Core–Shell Octahedra with High Activity toward Oxygen Reduction. *ACS Nano* **2014,** *8* (10), 10363-10371.
11. Wang, D.; Li, Y., Bimetallic Nanocrystals: Liquid-Phase Synthesis and Catalytic Applications. *Advanced Materials* **2011,** *23* (9), 1044-1060.
12. Nørskov, J. K.; Bligaard, T.; Rossmeisl, J.; Christensen, C. H., Towards the computational design of solid catalysts. *Nature Chemistry* **2009,** *1* (1), 37-46.
13. Nørskov, J. K.; Rossmeisl, J.; Logadottir, A.; Lindqvist, L.; Kitchin, J. R.; Bligaard, T.; Jónsson, H., Origin of the Overpotential for Oxygen Reduction at a Fuel-Cell Cathode. *The Journal of Physical Chemistry B* **2004,** *108* (46), 17886-17892.
14. Greeley, J.; Stephens, I. E. L.; Bondarenko, A. S.; Johansson, T. P.; Hansen, H. A.; Jaramillo, T. F.; Rossmeisl, J.; Chorkendorff, I.; Nørskov, J. K., Alloys of platinum and early transition metals as oxygen reduction electrocatalysts. *Nature Chemistry* **2009,** *1* (7), 552-556.
15. Corbierre, M. K.; Lennox, R. B., Preparation of Thiol-Capped Gold Nanoparticles by Chemical Reduction of Soluble Au(I)−Thiolates. *Chemistry of Materials* **2005,** *17* (23), 5691-5696.
16. Marbella, L. E.; Chevrier, D. M.; Tancini, P. D.; Shobayo, O.; Smith, A. M.; Johnston, K. A.; Andolina, C. M.; Zhang, P.; Mpourmpakis, G.; Millstone, J. E., Description and Role of Bimetallic Prenucleation Species in the Formation of Small Nanoparticle Alloys. *Journal of the American Chemical Society* **2015,** *137* (50), 15852-15858.
17. Bedford, N. M.; Showalter, A. R.; Woehl, T. J.; Hughes, Z. E.; Lee, S.; Reinhart, B.; Ertem, S. P.; Coughlin, E. B.; Ren, Y.; Walsh, T. R.; Bunker, B. A., Peptide-Directed PdAu Nanoscale Surface Segregation: Toward Controlled Bimetallic Architecture for Catalytic Materials. *ACS Nano* **2016,** *10* (9), 8645-8659.
18. Hofmann, D. M.; Fairbrother, D. H.; Hamers, R. J.; Murphy, C. J., Two-Phase Synthesis of Gold–Copper Bimetallic Nanoparticles of Tunable Composition: Toward Optimized Catalytic CO2 Reduction. *ACS Applied Nano Materials* **2019,** *2* (6), 3989-3998.
19. Royappa, A. T.; Tran, C. M.; Papoular, R. J.; Khan, M.; Marbella, L. E.; Millstone, J. E.; Gembicky, M.; Chen, B.; Shepard, W.; Elkaim, E., Copper(I) and gold(I) thiolate precursors to bimetallic nanoparticles. *Polyhedron* **2018,** *155*, 359-365.
20. Kahani, S. A.; Shahrokh, M., Synthesis of CuxNi1−x alloy nanoparticles from double complex salts and investigation of their magnetoimpedance effects. *RSC Advances* **2015,** *5* (88), 71601-71607.
21. Kahani, S. A.; Shahrokh, M., Preparation and characterization of Cu–Co alloy nanoparticles from double complex salts by chemical reduction. *New Journal of Chemistry* **2015,** *39* (10), 7916-7922.
22. Ding, K.; Cullen, D. A.; Zhang, L.; Cao, Z.; Roy, A. D.; Ivanov, I. N.; Cao, D., A general synthesis approach for supported bimetallic nanoparticles via surface inorganometallic chemistry. *Science* **2018,** *362* (6414), 560-564.
23. Samia, A. C. S.; Schlueter, J. A.; Jiang, J. S.; Bader, S. D.; Qin, C.-J.; Lin, X.-M., Effect of Ligand−Metal Interactions on the Growth of Transition-Metal and Alloy Nanoparticles. *Chemistry of Materials* **2006,** *18* (22), 5203-5212.
24. Yin, X.; Shi, M.; Wu, J.; Pan, Y.-T.; Gray, D. L.; Bertke, J. A.; Yang, H., Quantitative Analysis of Different Formation Modes of Platinum Nanocrystals Controlled by Ligand Chemistry. *Nano Letters* **2017,** *17* (10), 6146-6150.
25. Qin, F.; Ma, Y.; Miao, L.; Wang, Z.; Gan, L., Influence of Metal–Ligand Coordination on the Elemental Growth and Alloying Composition of Pt–Ni Octahedral Nanoparticles for Oxygen Reduction Electrocatalysis. *ACS Omega* **2019,** *4* (5), 8305-8311.
26. Asanova, T. I.; Asanov, I. P.; Kim, M. G.; Korenev, S. V., In situ X-ray spectroscopic investigation of thermal decomposition of double complex salt [Pt(NH3)4][OsCl6]. *Journal of Structural Chemistry* **2017,** *58* (5), 901-910.

27. Wu, S.; Li, M.; Sun, Y., In Situ Synchrotron X-ray Characterization Shining Light on the Nucleation and Growth Kinetics of Colloidal Nanoparticles. *Angewandte Chemie International Edition* **2019,** *0* (0).
28. Wu, L.; Fournier, A. P.; Willis, J. J.; Cargnello, M.; Tassone, C. J., In Situ X-ray Scattering Guides the Synthesis of Uniform PtSn Nanocrystals. *Nano letters* **2018,** *18* (6), 4053-4057.
29. Mi, J.-L.; Nørby, P.; Bremholm, M.; Becker, J.; Iversen, B. B., The formation mechanism of bimetallic PtRu alloy nanoparticles in solvothermal synthesis. *Nanoscale* **2015,** *7* (39), 16170-16174.
30. Chen, C.-H.; Hwang, B.-J.; Wang, G.-R.; Sarma, L. S.; Tang, M.-T.; Liu, D.-G.; Lee, J.-F., Nucleation and Growth Mechanism of Pd/Pt Bimetallic Clusters in Sodium Bis(2-ethylhexyl)sulfosuccinate (AOT) Reverse Micelles as Studied by in Situ X-ray Absorption Spectroscopy. *The Journal of Physical Chemistry B* **2005,** *109* (46), 21566-21575.
31. Zheng, H.; Smith, R. K.; Jun, Y.-w.; Kisielowski, C.; Dahmen, U.; Alivisatos, A. P., Observation of Single Colloidal Platinum Nanocrystal Growth Trajectories. *Science* **2009,** *324* (5932), 1309-1312.
32. Yuk, J. M.; Park, J.; Ercius, P.; Kim, K.; Hellebusch, D. J.; Crommie, M. F.; Lee, J. Y.; Zettl, A.; Alivisatos, A. P., High-Resolution EM of Colloidal Nanocrystal Growth Using Graphene Liquid Cells. *Science* **2012,** *336* (6077), 61-64.
33. Woehl, T. J.; Evans, J. E.; Arslan, I.; Ristenpart, W. D.; Browning, N. D., Direct in Situ Determination of the Mechanisms Controlling Nanoparticle Nucleation and Growth. *ACS Nano* **2012,** *6* (10), 8599-8610.
34. Alloyeau, D.; Dachraoui, W.; Javed, Y.; Belkahla, H.; Wang, G.; Lecoq, H.; Ammar, S.; Ersen, O.; Wisnet, A.; Gazeau, F.; Ricolleau, C., Unravelling Kinetic and Thermodynamic Effects on the Growth of Gold Nanoplates by Liquid Transmission Electron Microscopy. *Nano Letters* **2015,** *15* (4), 2574-2581.
35. Li, H.; Wang, L.; Dai, Y.; Pu, Z.; Lao, Z.; Chen, Y.; Wang, M.; Zheng, X.; Zhu, J.; Zhang, W.; Si, R.; Ma, C.; Zeng, J., Synergetic interaction between neighbouring platinum monomers in CO2 hydrogenation. *Nature nanotechnology* **2018,** *13* (5), 411-417.
36. Aliyah, K.; Lyu, J.; Goldmann, C.; Bizien, T.; Hamon, C.; Alloyeau, D.; Constantin, D., Real-Time In Situ Observations Reveal a Double Role for Ascorbic Acid in the Anisotropic Growth of Silver on Gold. *The journal of physical chemistry letters* **2020,** *11* (8), 2830-2837.
37. Abellan, P.; Parent, L. R.; Al Hasan, N.; Park, C.; Arslan, I.; Karim, A. M.; Evans, J. E.; Browning, N. D., Gaining Control over Radiolytic Synthesis of Uniform Sub-3-nanometer Palladium Nanoparticles: Use of Aromatic Liquids in the Electron Microscope. *Langmuir : the ACS journal of surfaces and colloids* **2016,** *32* (6), 1468-1477.
38. Hutzler, A.; Schmutzler, T.; Jank, M. P. M.; Branscheid, R.; Unruh, T.; Spiecker, E.; Frey, L., Unravelling the Mechanisms of Gold–Silver Core–Shell Nanostructure Formation by in Situ TEM Using an Advanced Liquid Cell Design. *Nano letters* **2018,** *18* (11), 7222-7229.
39. Park, J. H.; Schneider, N. M.; Grogan, J. M.; Reuter, M. C.; Bau, H. H.; Kodambaka, S.; Ross, F. M., Control of Electron Beam-Induced Au Nanocrystal Growth Kinetics through Solution Chemistry. *Nano letters* **2015,** *15* (8), 5314-5320.
40. Zhang, Y.; Keller, D.; Rossell, M. D.; Erni, R., Formation of Au Nanoparticles in Liquid Cell Transmission Electron Microscopy: From a Systematic Study to Engineered Nanostructures. *Chemistry of Materials* **2017,** *29* (24), 10518-10525.
41. Woehl, T. J., Metal Nanocrystal Formation during Liquid Phase Transmission Electron Microscopy: Thermodynamics and Kinetics of Precursor Conversion, Nucleation, and Growth. *Chemistry of Materials* **2020**, 10.1021/acs.chemmater.0c01360.
42. Hauwiller, M. R.; Ye, X., Tracking the Effects of Ligands on Oxidative Etching of Gold Nanorods in Graphene Liquid Cell Electron Microscopy. **2020,** *14* (8), 10239-10250.
43. Woehl, T. J.; Moser, T.; Evans, J. E.; Ross, F. M., Electron-beam-driven chemical processes during liquid phase transmission electron microscopy. *MRS Bulletin* **2020,** *45* (9), 746-753.

44. Birhanu, M. K.; Tsai, M.-C.; Chen, C.-T.; Kahsay, A. W.; Zeleke, T. S.; Ibrahim, K. B.; Huang, C.-J.; Liao, Y.-F.; Su, W.-N.; Hwang, B. J., Electrocatalytic reduction of carbon dioxide on gold–copper bimetallic nanoparticles: Effects of surface composition on selectivity. *Electrochimica Acta* **2020,** *356*, 136756.
45. Kim, D.; Resasco, J.; Yu, Y.; Asiri, A. M.; Yang, P., Synergistic geometric and electronic effects for electrochemical reduction of carbon dioxide using gold–copper bimetallic nanoparticles. *Nature Communications* **2014,** *5* (1), 4948.
46. Zhu, W.; Zhang, L.; Yang, P.; Hu, C.; Dong, H.; Zhao, Z.-J.; Mu, R.; Gong, J., Formation of Enriched Vacancies for Enhanced CO2 Electrocatalytic Reduction over AuCu Alloys. *ACS Energy Letters* **2018,** *3* (9), 2144-2149.
47. Sra, A. K.; Schaak, R. E., Synthesis of Atomically Ordered AuCu and AuCu3 Nanocrystals from Bimetallic Nanoparticle Precursors. *Journal of the American Chemical Society* **2004,** *126* (21), 6667-6672.
48. Chen, S.; Jenkins, S. V.; Tao, J.; Zhu, Y.; Chen, J., Anisotropic Seeded Growth of Cu–M (M = Au, Pt, or Pd) Bimetallic Nanorods with Tunable Optical and Catalytic Properties. *The Journal of Physical Chemistry C* **2013,** *117* (17), 8924-8932.
49. Andolina, C. M.; Dewar, A. C.; Smith, A. M.; Marbella, L. E.; Hartmann, M. J.; Millstone, J. E., Photoluminescent Gold–Copper Nanoparticle Alloys with Composition-Tunable Near-Infrared Emission. *Journal of the American Chemical Society* **2013,** *135* (14), 5266-5269.
50. Guisbiers, G.; Mejia-Rosales, S.; Khanal, S.; Ruiz-Zepeda, F.; Whetten, R. L.; José-Yacaman, M., Gold–Copper Nano-Alloy, "Tumbaga", in the Era of Nano: Phase Diagram and Segregation. *Nano Letters* **2014,** *14* (11), 6718-6726.
51. Tsuchida, E.; Nishide, H. In *Polymer-metal complexes and their catalytic activity*, Berlin, Heidelberg, Springer Berlin Heidelberg: Berlin, Heidelberg, 1977; pp 1-87.
52. Woehl, T. J.; Abellan, P., Defining the radiation chemistry during liquid cell electron microscopy to enable visualization of nanomaterial growth and degradation dynamics. *Journal of Microscopy* **2017,** *265* (2), 135-147.
53. Schneider, N. M.; Norton, M. M.; Mendel, B. J.; Grogan, J. M.; Ross, F. M.; Bau, H. H., Electron–Water Interactions and Implications for Liquid Cell Electron Microscopy. *The Journal of Physical Chemistry C* **2014,** *118* (38), 22373-22382.
54. Rodrigues, T. S.; Zhao, M.; Yang, T.-H.; Gilroy, K. D.; da Silva, A. G. M.; Camargo, P. H. C.; Xia, Y., Synthesis of Colloidal Metal Nanocrystals: A Comprehensive Review on the Reductants. *Chemistry – A European Journal* **2018,** *24* (64), 16944-16963.
55. Wang, M.; Dissanayake, T. U.; Park, C.; Gaskell, K.; Woehl, T. J., Nanoscale Mapping of Nonuniform Heterogeneous Nucleation Kinetics Mediated by Surface Chemistry. *Journal of the American Chemical Society* **2019,** *141* (34), 13516-13524.
56. Woehl, T. J.; Park, C.; Evans, J. E.; Arslan, I.; Ristenpart, W. D.; Browning, N. D., Direct Observation of Aggregative Nanoparticle Growth: Kinetic Modeling of the Size Distribution and Growth Rate. *Nano Letters* **2014,** *14* (1), 373-378.
57. Woehl, T. J., Metal Nanocrystal Formation during Liquid Phase Transmission Electron Microscopy: Thermodynamics and Kinetics of Precursor Conversion, Nucleation, and Growth. *Chemistry of Materials* **2020,** *32* (18), 7569-7581.
58. Qian, Y.; Huang, J. Z.; Ding, Y., Identifying multi-stage nanocrystal growth using in situ TEM video data. *IISE Transactions* **2017,** *49* (5), 532-543.
59. Handwerk, D. R.; Shipman, P. D.; Whitehead, C. B.; Özkar, S.; Finke, R. G., Particle Size Distributions via Mechanism-Enabled Population Balance Modeling. *The Journal of Physical Chemistry C* **2020,** *124* (8), 4852-4880.
60. Hoffman, M. Z.; Hayon, E., Pulse radiolysis study of sulfhydryl compounds in aqueous solution. *The Journal of Physical Chemistry* **1973,** *77* (8), 990-996.

61. Tung, T.-L.; Kuntz, R. R., The Reactions of Hydrogen Atoms in Aqueous Solutions: Thiols. *Radiation Research* **1973,** *55* (1), 10-17.
62. Tamba, M.; Simone, G.; Quintiliani, M., Interactions of Thiyl Free Radicals with Oxygen: A Pulse Radiolysis Study. *International Journal of Radiation Biology and Related Studies in Physics, Chemistry and Medicine* **1986,** *50* (4), 595-600.
63. Hoffman, M. Z.; Hayon, E., One-electron reduction of the disulfide linkage in aqueous solution. Formation, protonation, and decay kinetics of the RSSR- radical. *Journal of the American Chemical Society* **1972,** *94* (23), 7950-7957.
64. Matheson, M. S.; Mamou, A.; Silverman, J.; Rabani, J., Reaction of hydroxyl radicals with polyethylene oxide in aqueous solution. *The Journal of Physical Chemistry* **1973,** *77* (20), 2420-2424.
65. Gnanasekaran, K.; Vailonis, K. M.; Jenkins, D. M.; Gianneschi, N. C., In Situ Monitoring of the Seeding and Growth of Silver Metal–Organic Nanotubes by Liquid-Cell Transmission Electron Microscopy. *ACS Nano* **2020,** *14* (7), 8735-8743.
66. Love, J. C.; Estroff, L. A.; Kriebel, J. K.; Nuzzo, R. G.; Whitesides, G. M., Self-Assembled Monolayers of Thiolates on Metals as a Form of Nanotechnology. *Chemical Reviews* **2005,** *105* (4), 1103-1170.
67. Xue, Y.; Li, X.; Li, H.; Zhang, W., Quantifying thiol–gold interactions towards the efficient strength control. *Nature communications* **2014,** *5* (1), 4348.
68. Grönbeck, H.; Curioni, A.; Andreoni, W., Thiols and Disulfides on the Au(111) Surface: The Headgroup−Gold Interaction. *Journal of the American Chemical Society* **2000,** *122* (16), 3839-3842.
69. Remita, H.; Etcheberry, A.; Belloni, J., Dose Rate Effect on Bimetallic Gold−Palladium Cluster Structure. *The Journal of Physical Chemistry B* **2003,** *107* (1), 31-36.
70. Belloni, J.; Mostafavi, M.; Remita, H.; Marignier, J.-L.; Marie-Odile Delcourt, a., Radiation-induced synthesis of mono- and multi-metallic clusters and nanocolloids. *New Journal of Chemistry* **1998,** *22* (11), 1239-1255.
71. Kauko, H.; Grieb, T.; Bjørge, R.; Schowalter, M.; Munshi, A. M.; Weman, H.; Rosenauer, A.; van Helvoort, A. T. J., Compositional characterization of GaAs/GaAsSb nanowires by quantitative HAADF-STEM. *Micron* **2013,** *44*, 254-260.
72. House, S. D.; Chen, Y.; Jin, R.; Yang, J. C., High-throughput, semi-automated quantitative STEM mass measurement of supported metal nanoparticles using a conventional TEM/STEM. *Ultramicroscopy* **2017,** *182*, 145-155.
73. Liao, T. W.; Yadav, A.; Hu, K. J.; van der Tol, J.; Cosentino, S.; D'Acapito, F.; Palmer, R. E.; Lenardi, C.; Ferrando, R.; Grandjean, D.; Lievens, P., Unravelling the nucleation mechanism of bimetallic nanoparticles with composition-tunable core-shell arrangement. *Nanoscale* **2018,** *10* (14), 6684-6694.
74. Gary, D. C.; Terban, M. W.; Billinge, S. J. L.; Cossairt, B. M., Two-Step Nucleation and Growth of InP Quantum Dots via Magic-Sized Cluster Intermediates. *Chemistry of Materials* **2015,** *27* (4), 1432-1441.
75. Luo, Z.; Nachammai, V.; Zhang, B.; Yan, N.; Leong, D. T.; Jiang, D.-e.; Xie, J., Toward Understanding the Growth Mechanism: Tracing All Stable Intermediate Species from Reduction of Au(I)–Thiolate Complexes to Evolution of Au25 Nanoclusters. *Journal of the American Chemical Society* **2014,** *136* (30), 10577-10580.
76. Chen, T.; Fung, V.; Yao, Q.; Luo, Z.; Jiang, D.-e.; Xie, J., Synthesis of Water-Soluble [Au25(SR)18]− Using a Stoichiometric Amount of NaBH4. *Journal of the American Chemical Society* **2018,** *140* (36), 11370-11377.
77. Dar, W. A.; Bodiuzzaman, M.; Ghosh, D.; Paramasivam, G.; Khatun, E.; Sugi, K. S.; Pradeep, T., Interparticle Reactions between Silver Nanoclusters Leading to Product Cocrystals by Selective Cocrystallization. *ACS Nano* **2019,** *13* (11), 13365-13373.
78. Aslan, M.; Davis, J. B. A.; Johnston, R. L., Global optimization of small bimetallic Pd–Co binary nanoalloy clusters: a genetic algorithm approach at the DFT level. *Physical Chemistry Chemical Physics* **2016,** *18* (9), 6676-6682.

79. Pittaway, F.; Paz-Borbón, L. O.; Johnston, R. L.; Arslan, H.; Ferrando, R.; Mottet, C.; Barcaro, G.; Fortunelli, A., Theoretical Studies of Palladium−Gold Nanoclusters: Pd−Au Clusters with up to 50 Atoms. *The Journal of Physical Chemistry C* **2009,** *113* (21), 9141-9152.
80. Molayem, M.; Grigoryan, V. G.; Springborg, M., Theoretical Determination of the Most Stable Structures of NimAgn Bimetallic Nanoalloys. *The Journal of Physical Chemistry C* **2011,** *115* (15), 7179-7192.
81. Molayem, M.; Grigoryan, V. G.; Springborg, M., Global Minimum Structures and Magic Clusters of CumAgn Nanoalloys. *The Journal of Physical Chemistry C* **2011,** *115* (45), 22148-22162.
82. Chen, J.; Jiang, T.; Wei, G.; Mohamed, A. A.; Homrighausen, C.; Krause Bauer, J. A.; Bruce, A. E.; Bruce, M. R. M., Electrochemical and Chemical Oxidation of Gold(I) Thiolate Phosphine Complexes: Formation of Gold Clusters and Disulfide. *Journal of the American Chemical Society* **1999,** *121* (39), 9225-9226.
83. Moser, T. H.; Mehta, H.; Park, C.; Kelly, R. T.; Shokuhfar, T.; Evans, J. E., The role of electron irradiation history in liquid cell transmission electron microscopy. *Science Advances* **2018,** *4* (4), eaaq1202.
84. Abellan, P.; Woehl, T. J.; Parent, L. R.; Browning, N. D.; Evans, J. E.; Arslan, I., Factors influencing quantitative liquid (scanning) transmission electron microscopy. *Chemical Communications* **2014,** *50* (38), 4873-4880.
85. Williams, D. B.; Carter, C. B., Transmission electron microscopy : a textbook for materials science. 2nd ed. ed.; Springer: New York, 2009.
86. Sheridan, P. J., Determination of experimental and theoretical kASi factors for a 200-kV analytical electron microscope. *Journal of Electron Microscopy Technique* **1989,** *11* (1), 41-61.
87. Neta, P.; Schuler, R. H., Rate Constants for Reaction of Hydrogen Atoms with Compounds of Biochemical Interest. *Radiation Research* **1971,** *47* (3), 612-627.

FIGURES

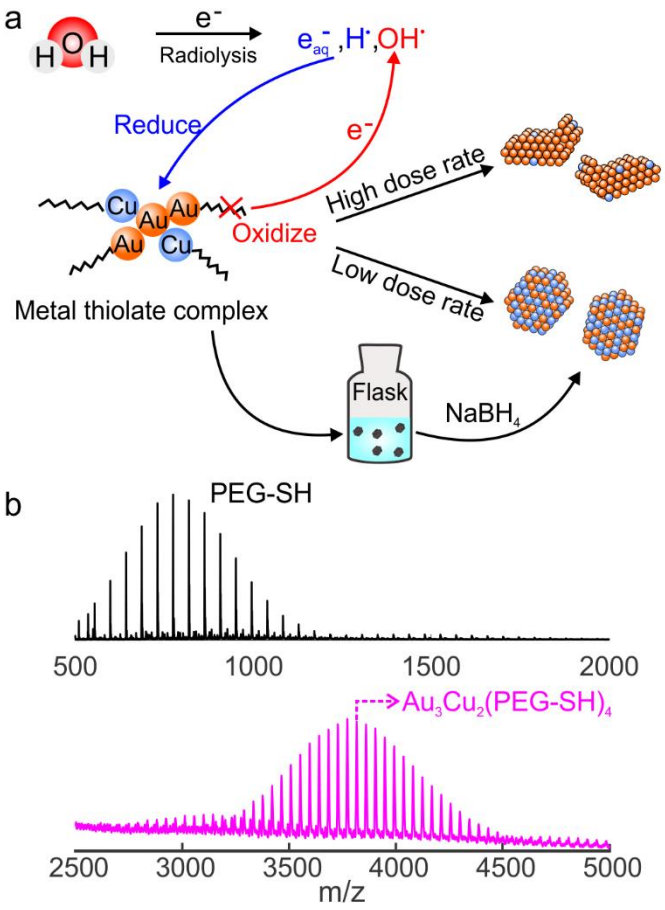

Figure 1. (a) Schematic of *in situ* LP-TEM synthesis and *ex situ* flask synthesis of AuCu nanoparticles from metal thiolate complexes. (b) Top: MALDI-TOF MS of poly(ethylene glycol) methyl ether thiol (PEG-SH, average MW ≈ 775 g/mol). Bottom: MALDI-TOF MS of PEG-SH mixed with $HAuCl_4$ and $Cu(NO_3)_2$.

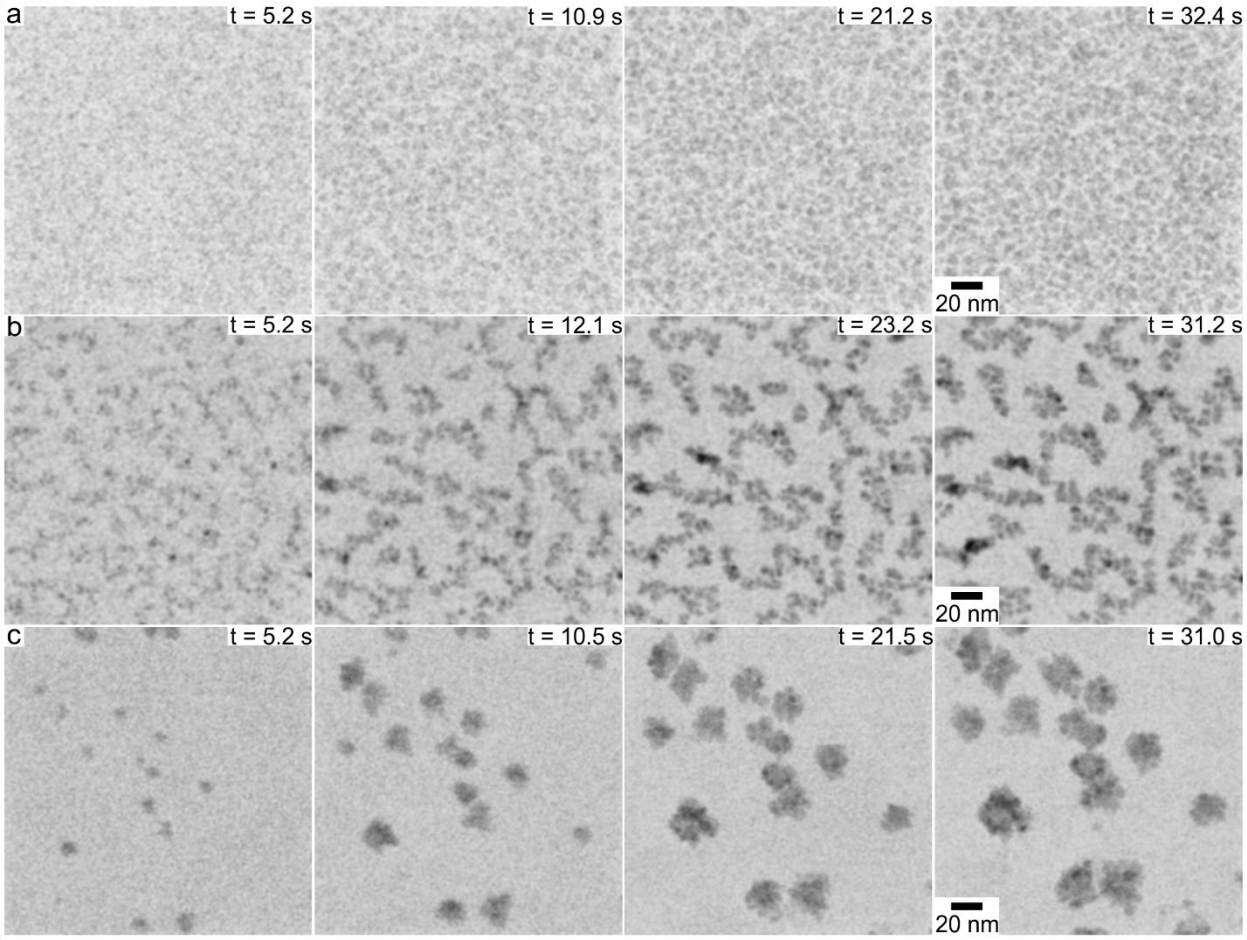

Figure 2. Time lapsed LP-TEM images (bright field STEM) of AuCu nanocrystal formation. (a) Nanocrystal formation from metal thiolate complexes at a magnification of 500,000 and beam current of 16 pA (dose rate of 17 MGy/s). (b) Nanocrystal formation from metal thiolate complexes at a magnification of 400,000 and beam current of 141 pA (dose rate of 65 MGy/s). (c) Nanocrystal formation from a physical mixture of $HAuCl_4$ and $Cu(NO_3)_2$ at a magnification of 400,000 and beam current of 141 pA (dose rate of 65 MGy/s).

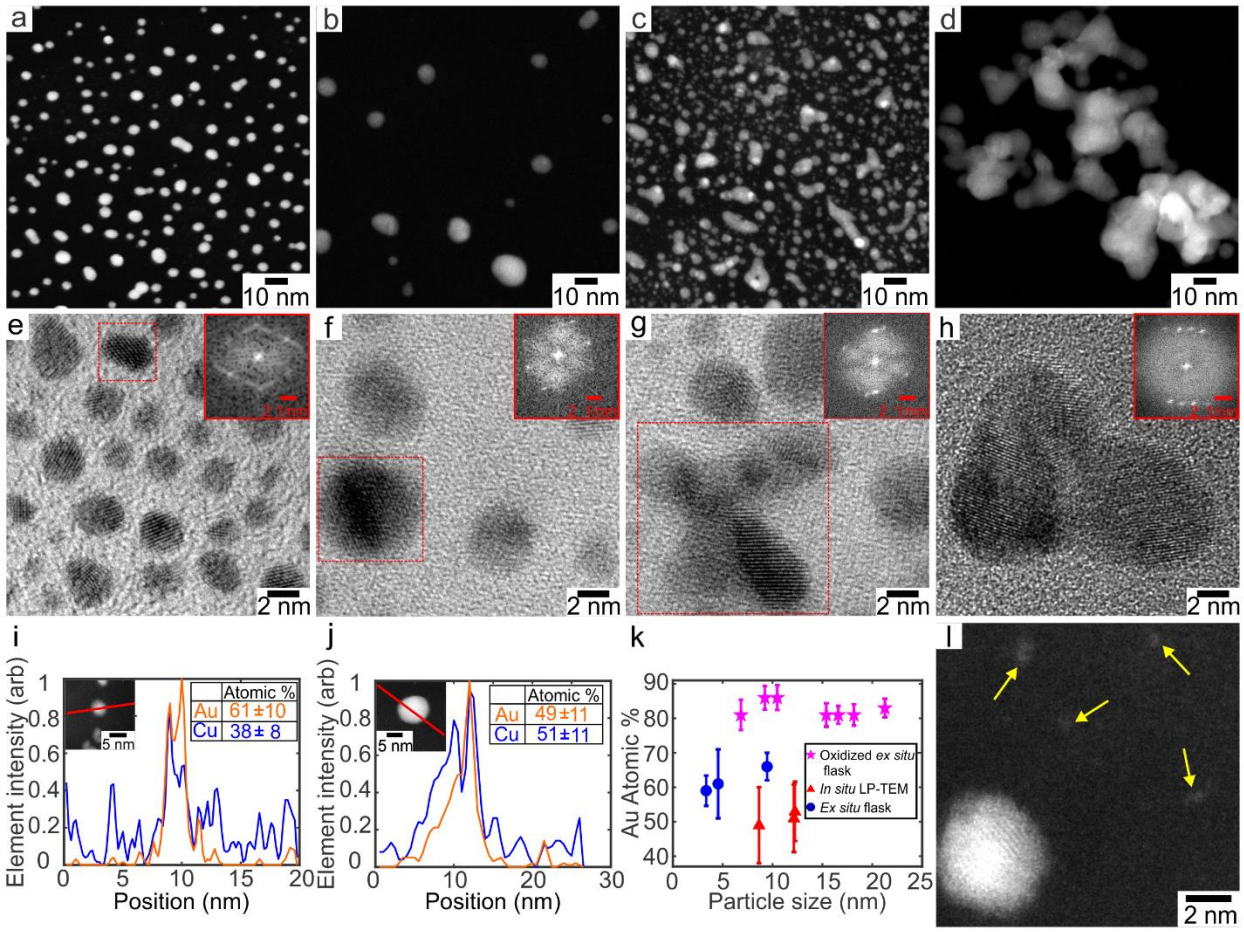

Figure 3. Characterization of nanocrystals synthesized by *in situ* LP-TEM synthesis and *ex situ* flask synthesis using HAADF-STEM (top row), HRTEM (middle row), and STEM-EDS (i-k). (a),(e),(i) Nanocrystals synthesized by *ex situ* flask synthesis. (b),(f),(j) Nanocrystals synthesized by *in situ* LP-TEM synthesis from metal thiolate complexes at a magnification of 400,000 and beam current of 16 pA (dose rate of 7.3 MGy/s). (c),(g) Nanocrystals synthesized by LP-TEM from metal thiolate complexes at a magnification of 600,000 and beam current of 141 pA (dose rate of 210 MGy/s). (d),(h) Nanocrystals synthesized by LP-TEM from a physical mixture of $HAuCl_4$ and $Cu(NO_3)_2$ at a magnification of 400,000 and beam current of 23 pA (dose rate of 10 MGy/s). (k) Gold atomic percent as a function of particle size for different synthesis conditions shown in the legend (*ex situ* flask synthesis, *ex situ* flask synthesis from oxidized precursor, and

low dose rate *in situ* LP-TEM synthesis). (l) HAADF-STEM image showing sub-nanometer metal clusters (yellow arrows).

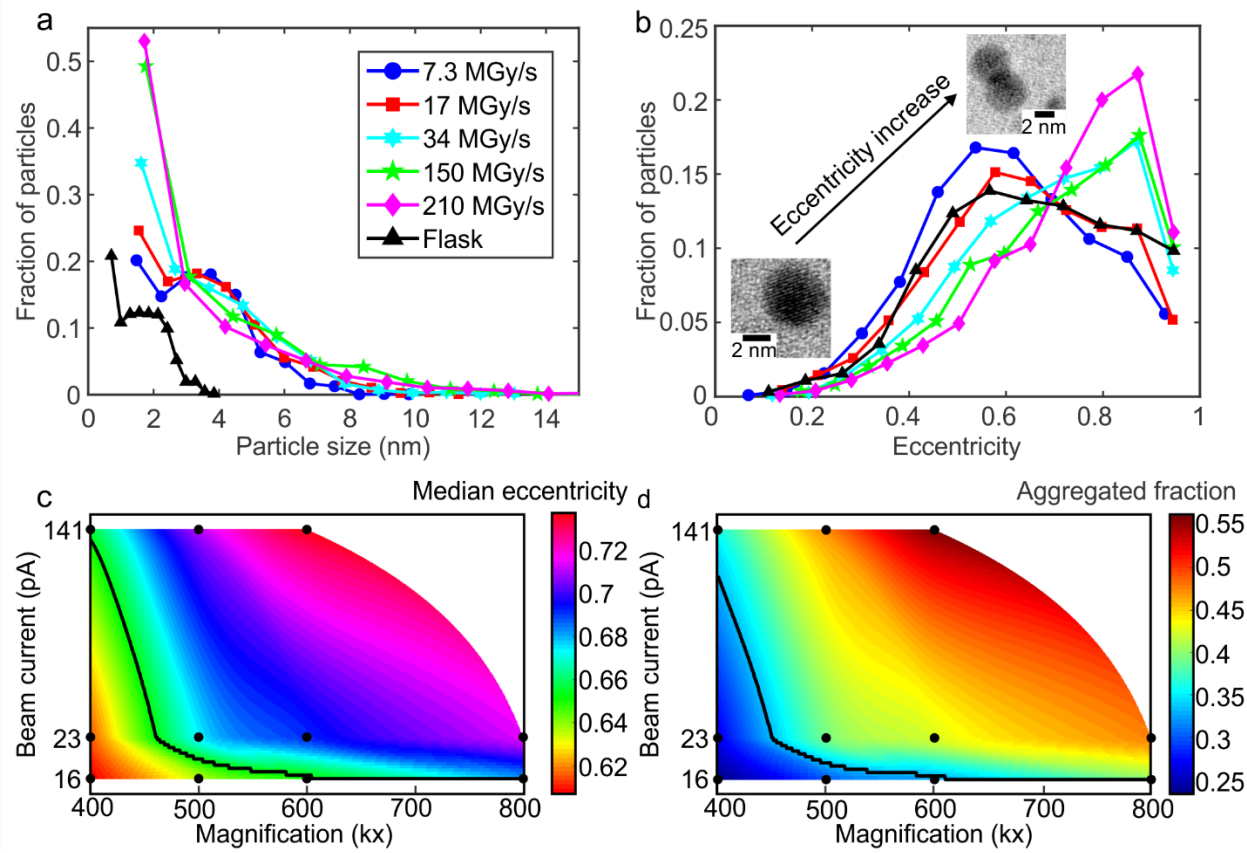

Figure 4. (a) Particle size distributions and (b) eccentricity distributions of nanocrystals formed by *in situ* LP-TEM synthesis at different dose rates compared to *ex situ* flask synthesis. Heat maps of (c) eccentricity and (d) aggregated fraction for *in situ* LP-TEM synthesis as a function of magnification and beam current. Black dots in (c) and (d) show the experimental conditions where measurements were taken. Black curves of constant eccentricity and aggregated fraction corresponding to nanocrystals synthesized by *ex situ* flask synthesis are shown in (c) and (d).

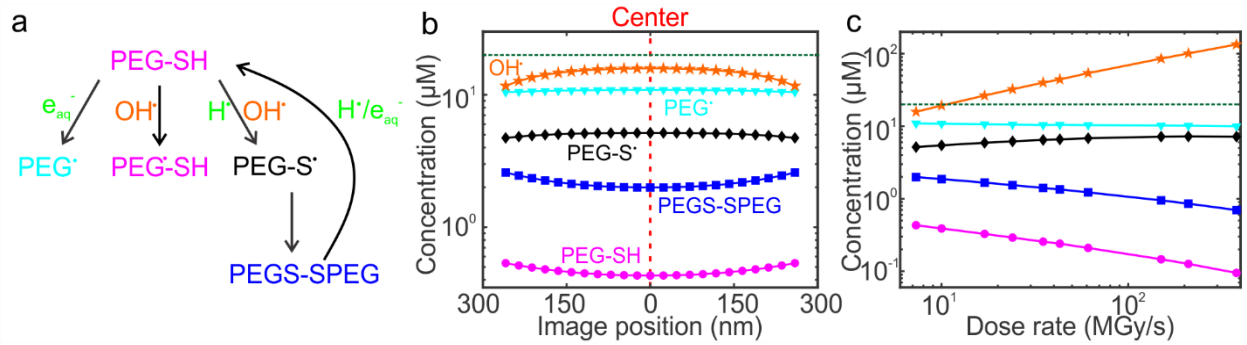

Figure 5. (a) Schematic showing radical-ligand reaction pathways. PEG · −SH (center pathway) undergoes the same oxidation/reduction cycle as PEG − S ·, but it is not pictured for simplicity. (b) Steady state concentration of radical species as a function position within the LP-TEM image area for a magnification of 400,000, beam current of 16 pA (dose rate of 7.3 MGy/s). (c) Steady state concentration of each radical and ligand damage species at the center of the LP-TEM image area as a function of dose rate. The horizontal dashed green lines show the 20 μM initial concentration of PEG-SH.

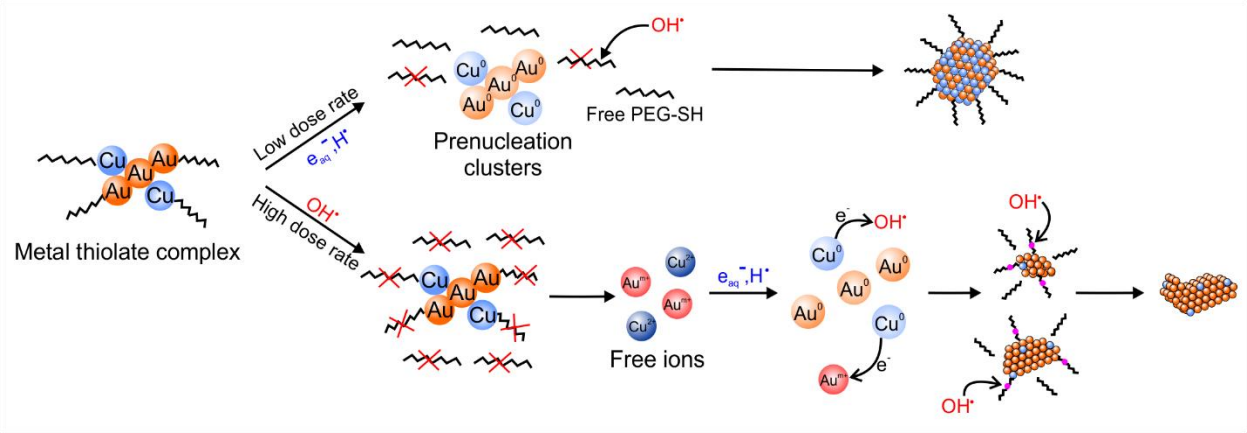

Figure 6. Schematic showing the overall mechanism for ligand and dose rate-mediated nanocrystal formation during *in situ* LP-TEM synthesis.